第 39 卷 第 3 期　　新 型 炭 材 料（中英文）　　Vol. 39 No. 3
2024 年 6 月　　NEW CARBON MATERIALS　　Jun. 2024

Sulfonyl chloride-intensified metal chloride intercalation of graphite for efficient sodium storage

LAN Shu-qin[1,†], REN Wei-cheng[1,†], WANG Zhao[1,2,*], YU Chang[1,*], YU Jin-he[1], LIU Ying-bin[1], XIE Yuan-yang[1], ZHANG Xiu-bo[1], WANG Jian-jian[1], QIU Jie-shan[3,*]

（1. *State Key Laboratory of Fine Chemicals*, *School of Chemical Engineering*, *Dalian University of Technology*, *Dalian* 116024, *China*;
2. *College of Chemistry and Material Science*, *Shandong Agricultural University*, *Tai'an* 271018, *China*;
3. *State Key Laboratory of Chemical Resource Engineering*, *College of Chemical Engineering*, *Beijing University of Chemical Technology*, *Beijing* 100029, *China*）

Abstract: Metal chloride-intercalated graphite with excellent conductivity and a large interlayer spacing is highly desired for use in sodium ion batteries. However, halogen vapor is usually indispensable in initiating the intercalation process, which makes equipment design and experiments challenging. In this work, SO_2Cl_2 was used as a chlorine generator to intensify the intercalation of $BiCl_3$ into graphite ($BiCl_3$-GICs), which avoided the potential risks, such as Cl_2 leakage, in traditional methods. The operational efficiency in the experiment was also improved. After the reaction of SO_2Cl_2, $BiCl_3$, and graphite at 200 °C for 20 h, the synthesized $BiCl_3$-GICs had a large interlayer spacing (1.26 nm) and a high amount of $BiCl_3$ intercalation (42%), which gave SIBs a high specific capacity of 213 mAh g^{-1} at 1 A g^{-1} and an excellent rate performance (170 mAh g^{-1} at 5 A g^{-1}). In-situ Raman spectra revealed that the electronic interaction between graphite and intercalated $BiCl_3$ is weakened during the first discharge, which is favorable for sodium storage. This work broadly enables the increased intercalation of other metal chloride-intercalated graphites, offering possibilities for developing advanced energy storage devices.

Key words: Chlorine generator; Metal chloride-intercalated graphite; Intercalation intensification process; Anode material; Sodium-ion batteries

1 Introduction

Sodium-ion batteries (SIBs) have garnered significant interest from researchers due to the practically abundant sodium supplies, good reversibility, and respectable energy density[1–4]. Therefore, significant research has been conducted to explore advanced anode materials for SIBs such as phosphorus[5], metal oxides[6], and carbon-based materials[7–12]. Among these materials, carbon materials have been proposed as prospective anode materials since carbon is abundantly available, and exhibits high specific capacity, low redox potential and excellent chemical stability[13–15]. Benefiting from the weak interlayer interaction and the distinctive layered structure, graphite with excellent conductivity and satisfactory stability, has been extensively employed as the common natural carbon material in energy storage devices[16]. However, due to the mismatch of graphite lattices and sodium ions, graphite can only deliver a low capacity of 35 mAh g^{-1}[17]. As such, the development of high-performance carbon-based electrode materials require critical attention to boost the energy storage capacity of SIBs[18].

As a typical example of graphite-based materials, metal chloride-intercalated graphite possesses exceptional physical and chemical properties[19]. First, the conductivity of metal chloride-intercalated graphite is improved due to the hole-doping effect of metal chloride towards graphite layers. Furthermore, the energy barrier of sodium ions diffusion can be reduced due to the enlarged interlayer spacing and the adjusted ion migration path. In addition, the dense structure of ori-

---

Received date: 2023-11-18; **Revised date:** 2024-03-29

Corresponding author: WANG Zhao. E-mail: wangzhao3709@sdau.edu.cn;
YU Chang. E-mail: chang.yu@dlut.edu.cn;
QIU Jie-shan. E-mail: qiujs@mail.buct.edu.cn

Author introduction: †LAN Shu-qin and REN Wei-cheng were contributed equally to this work

ginal graphite is maintained, which can be of great benefit to improve the volumetric performance. Especially, some metal chlorides, such as those based on Mo, Sn, Bi and Ge metal chlorides, usually possess high theoretical capacities due to the multi-electron conversion or conversion-alloying reaction with the sodium ions. Intercalating graphite with these metal chlorides is an effective method to produce advanced carbon-based materials for SIBs[20,21]. Li et al. demonstrated that the molybdenum pentachloride-graphite intercalation compounds ($MoCl_5$–GICs), used as the anode material for SIB, delivered a capacity retention of 27%. Specifically, they achieved a specific capacity of 271 at 0.2 A g^{-1}, while at a higher current density of 5 A g^{-1}, the specific capacity decreased to 72 mAh g^{-1}[21]. Li et al. proposed that an $AlCl_3$-GICs as the anode material of SIB exhibited a capacity retention of 32% upon increasing the current density; 259 mAh g^{-1} at 0.2 A g^{-1} quickly reduced to 83 mAh g^{-1} at 5 A g^{-1}[22]. Therefore, the rate performance of these metal chloride-intercalated graphite need further improvement. Moreover, the pressure threshold of halogen vapor always is a crucial factor to determine the operational efficiency in experiment[23,24]. Consequently, the synthesis of metal chloride-intercalated graphite is restricted by the sluggish intercalation reaction and the unsafe synthesis conditions in most cases. Developing an innovative approach to avoid the utilization of chlorine vapor and promote the application of metal chloride-intercalated graphite.

In this work, SO_2Cl_2 was firstly employed as chlorine generator to intensify the $BiCl_3$ intercalation process. The impact of reaction conditions (temperature and time) on the structure of metal chloride-intercalated graphite with regard to the interlayer spacing and content of $BiCl_3$ was systematically explored. It was discovered that the interlayer spacing of as-synthesized $BiCl_3$-graphite intercalation compounds ($BiCl_3$-GICs) was enlarged to 1.26 nm, accompanying with a high $BiCl_3$ mass content of 42%. Owing to the distinctive structure, the $BiCl_3$-GICs delivered a high specific capacity (213 mAh g^{-1} at 1 A g^{-1}) and fantastic rate performance (170 mAh g^{-1} at 5 A g^{-1}), the capacity retention rate reached up to 80%. Furthermore, the in-situ Raman technique revealed that electronic interaction between graphite and the intercalated $BiCl_3$ is weakened during the first discharge, which is favorable for the sodium storage. Also, the SO_2Cl_2-intensified strategy can be successfully extended to other metal metal chloride[25]. The intercalation intensification process enabled by SO_2Cl_2 in this work pave the way for developing the advanced metal chloride-intercalated graphite with superior energy storage performance.

2 Experimental section

2.1 Preparation of $BiCl_3$-GICs

In a glove box, $BiCl_3$ and graphite were mixed at a mass of 0.2 and 1.0 g, respectively. After adding 750 μL SO_2Cl_2, the mixture was evenly pulverized and placed into a stainless steel reactor. Subsequently, the raw material was heated to 200 °C with a 5 °C min^{-1} rate and maintained for 20 h. Following that, the sample was cooled to 25 °C and subsequently cleaned for 4 h with a solution of 2 mol L^{-1} HCl and rinsed with deionized water until neutral. After filtering, the sample was vacuum-dried at 80 °C to extract the $BiCl_3$-GICs. The best technological conditions were explored by changing the reaction temperature (100, 150, 200, 300 and 450 °C) and reaction time (10, 20 and 30 h). Moreover, the molybdenum pentachloride-graphite intercalation compounds ($MoCl_5$-GICs) and tungsten hexachloride-graphite intercalation compounds (WCl_6-GICs) were fabricated according to the same method by replacing $BiCl_3$ with $MoCl_5$ and WCl_6, respectively.

2.2 Micro-structure and properties characterization

The micro-structure of $BiCl_3$-GICs was analyzed by the powder X-ray diffraction (XRD, Cu *K*α, λ= 1.540 6 Å), Raman spectroscopy (LabRAM HR Evolution Raman Microscope, HORIBA, 532 nm), and Fourier transform infrared spectroscopy (FT-IR, Bruker INVENIO-R spectrometer, ATR). The amount of $BiCl_3$ in $BiCl_3$-GICs was calculated from the results of thermogravimetric analysis (TGA, STA 449 F3) test. The scanning electron microscopy (SEM, HITACHI UHR FE-SEM SU8220) and transmission electron microscopy (TEM, FEI TF30) were applied to characterize the morphology of samples. The chemical components of $BiCl_3$-GICs were identified by the X-ray photoelectron spectroscopy (XPS, Thermo ESCALAB 250).

The $BiCl_3$-GICs, conductive agent, and binder were blended with the 8 : 1 : 1 mass ratio to prepare the anode electrode, followed by thorough grinding after adding appropriate quantity of binder. Then the resulting homogeneous mixture was coated on Cu foil with a 100 μm thickness and subsequently vacuum-dried for 12 h at 80 °C. The anode electrode, separator (Whatman GF/D), sodium foil, and commercial electrolyte (sodium hexafluorophosphate dissolved in ethylene carbonate and dimethyl carbonate, 1 mol L^{-1}) were applied to assemble the half cell. After the cell was left standing for 12 h, the galvanostatic charge/discharge (GCD) test was conducted by the Land battery test system (CT2001A), the cyclic voltammetry (CV) test was conducted by IVIUM electrochemical workstation, and the electrochemical impedance spectroscopy (EIS) was analyzed by the VSP electrochemical workstation at 25±1 °C.

3 Results and discussion

The proposed synthesis route of $BiCl_3$-GICs is clearly illustrated in Fig. 1. Conventionally, Cl_2 has been used to facilitate the intercalation process of $BiCl_3$, posing safety risks due to its toxicity. In this work, SO_2Cl_2 was innovatively used as chlorine generator to enhance the operational efficiency in the experiment. The SO_2Cl_2 acted as a Cl_2 generator and decomposed in-situ to produce Cl_2 during the heating process. This contributed to an expansion of the graphite interlayer spacing from 0.34 to 1.26 nm, accelerating the rapid diffusion of $BiCl_3$ within the graphite layers and thus promoting the synthesis of $BiCl_3$-GICs.

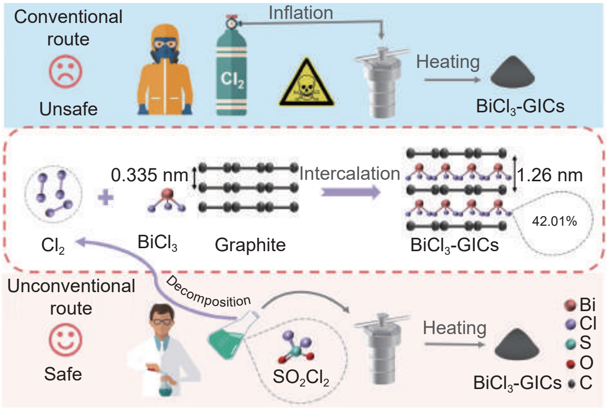

Fig. 1 Schematic diagram for the formation of $BiCl_3$-GICs

The effect of reaction temperature and reaction time on the interlayer spacing and the amount of intercalated $BiCl_3$ in $BiCl_3$-GICs were investigated by the XRD and TGA test. At a reaction temperature of 100 °C, there is a distinctive diffraction peak of graphite (002) crystal plane, whereas the weak diffraction peak at 12.1° was attributed to the BiOCl impurity arising from the hydrolysis product of the residual $BiCl_3$ during washing[26] (Fig. 2a). At 150 °C, the diffraction peaks at 7.0°, 13.7°, 20.5° and 27.4° belong to the (001), (002), (003) and (004) crystal planes of the stage-2 intercalation phase, respectively, indicating the formation of stage-2 intercalation phase. At 200 and 300 °C, the new diffraction peaks at 9.2° and 18.3° attribute to the (001) and (002) crystal planes of the stage-1 intercalation phase, respectively. Correspondingly, both stage-1 and stage-2 intercalation phase diffraction peaks are present, but the intensities of the stage-1 intercalation phase diffraction peaks are more sharp for the $BiCl_3$-GICs synthesized at 200 °C compared that at 300 °C. When the temperature increases to 450 °C, the intensities of diffraction peaks corresponding to both stage-1 and stage-2 intercalation phase are weakened, attributing to the degradation of $BiCl_3$-GICs at high temperature. The TGA curves (Fig. 2b) demonstrate that the weight loss starts at 600 °C for graphite and the oxidation and complete conversion of graphite at 900 °C. For the $BiCl_3$-GICs, an obvious weight loss starts at 220 °C, attributed to the escape of partial $BiCl_3$ in the $BiCl_3$-GICs. Subsequently, the residual $BiCl_3$ can be oxidized into Bi_2O_3 at 600 °C along with the removal of graphite. Based on this, the mass fraction of $BiCl_3$ (C_{BiCl_3}) in $BiCl_3$-GICs was calculated based on the formula:

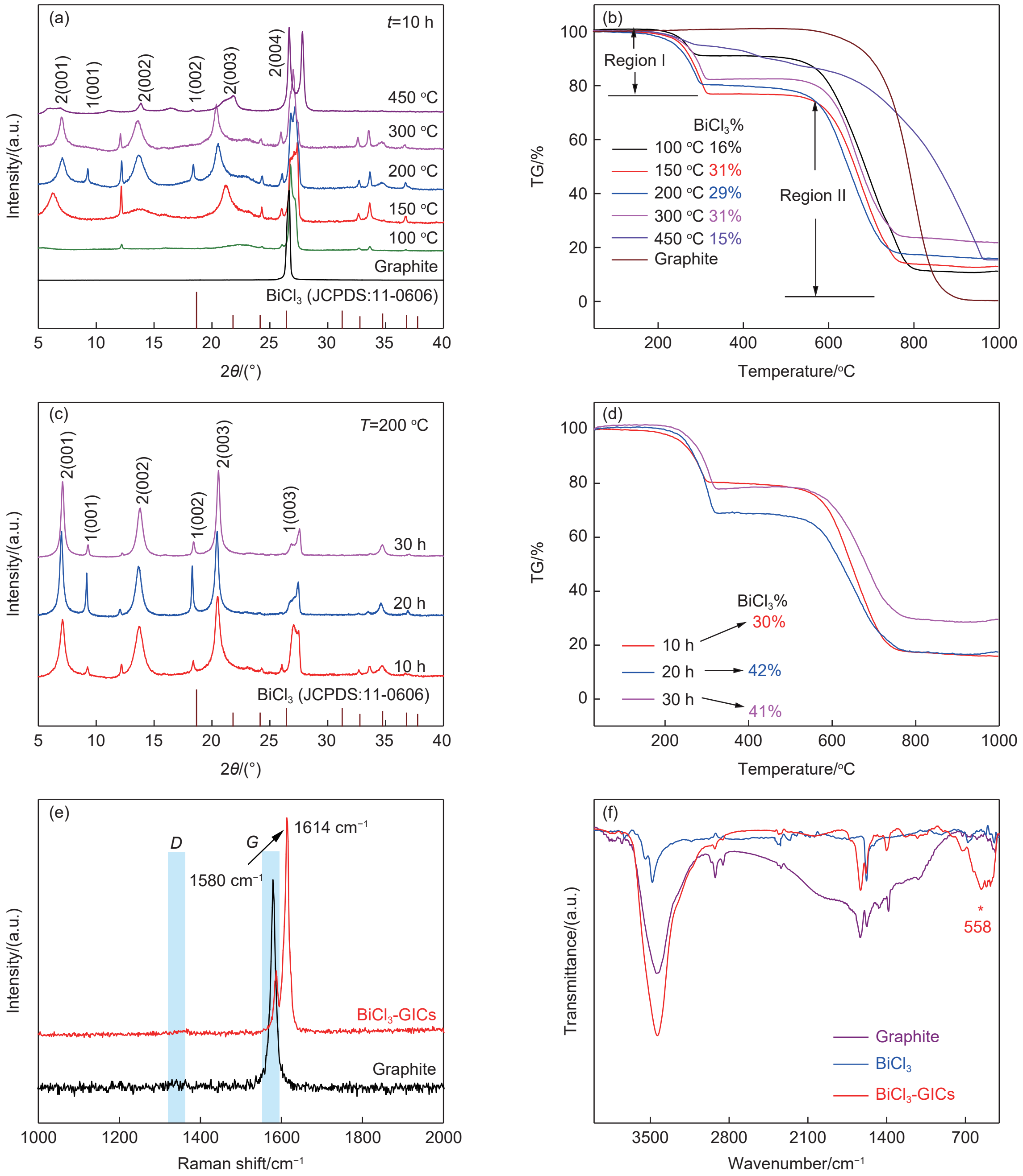

Fig. 2　(a) XRD patterns and (b) TGA curves of the $BiCl_3$-GICs samples fabricated at various temperatures (reaction time: 10 h). (c) XRD patterns and (d) TGA curves of the $BiCl_3$-GICs samples prepared at various reaction times (reaction temperature: 200 °C). (e) Raman spectra and (f) FT-IR spectra of graphite and the $BiCl_3$-GICs

$$C_{BiCl_3}(\%) = C_{I}(\%) + \frac{C_{II}(\%)}{M_{(Bi)_2O_3}} M_{(BiCl_3)}$$

where C_I and C_{II} are the ratio of weight loss for the region I and region II, respectively. $M_{(Bi_2Cl_3)}$ and $M_{(BiCl_3)}$ are the mole mass of Bi_2O_3 and $BiCl_3$, respectively. The as-fabricated $BiCl_3$-GICs at 100 and 450 °C present low $BiCl_3$ contents, being 16% and 15%, respectively. Also, it is noted that there is high $BiCl_3$ content and little difference in the $BiCl_3$ contents of the $BiCl_3$-GICs synthesized at 200 and 300 °C. Thus, to prepare $BiCl_3$-GICs at a relatively low temperature of 200 °C is a wise choice to save energy.

Reaction time is another key factor affecting the intercalation structure. In general, a more thorough intercalation reaction occurs with the increase of reaction time. However, if the intercalation process reaches an equilibrium state, $BiCl_3$ cannot intercalate into the graphite layers. Therefore, the proper reaction time must be discovered to ensure the intercalation equilibrium. As shown in Fig. 2c, the intensities of the diffraction peaks corresponding to intercalation phase were enhanced with an increase in reaction time from 10 to 20 h, implying the obviously increased intercalation content of $BiCl_3$. In addition, the diffraction peaks of stage-2 intercalation phase are more obvious than that of stage-1 phase, suggesting that the stage-2 intercalation phase dominates the $BiCl_3$-GICs. When the reaction time was prolonged to 30 h, the intensities of diffraction peaks for the stage-1 intercalation phase were weakened but that of the stage-2 intercalation phase were intensified, which can be attributed to the transformation of intercalation phase from the stage-1 to the stage-2. This is confirmed by the TGA results (Fig. 2d). The highest intercalation amount (42%) of $BiCl_3$ toward graphite occurs at 200 °C and 20 h.

The intercalation of metal chloride toward graphite may lead to the shift of conjugated π electrons of graphite layers to the metal chloride, reflecting as a blue shift of *G* peak for graphite in Raman spectra[27]. Compared with graphite, the *G* peak of $BiCl_3$-GICs exhibits a blue shift from 1 580 to 1 614 cm^{-1}, verifying the successful intercalation of $BiCl_3$ into graphite layers (Fig. 2e). In addition, the intensity of *D* peak in $BiCl_3$-GICs has almost no change compared with that of graphite, verifying that the intercalation of $BiCl_3$ does not introduce defects to the structure of graphite. Furthermore, the distinct peak at 558 cm^{-1} for $BiCl_3$-GICs, which is attributed to the C—Cl bond stretching vibration[28,29], reveals the intensive interaction between $BiCl_3$ and the graphite layers (Fig. 2f).

The valence state of the $BiCl_3$-GICs sample was detected and analyzed by XPS. According to the full XPS survey spectrum (Fig. 3a), there are C, O, Bi and Cl elements in the $BiCl_3$-GICs. As shown in Fig. 3b, there are 2 peaks located at 284.8 and 286.0 eV in C 1s, which can be attributed to the C—C bond and

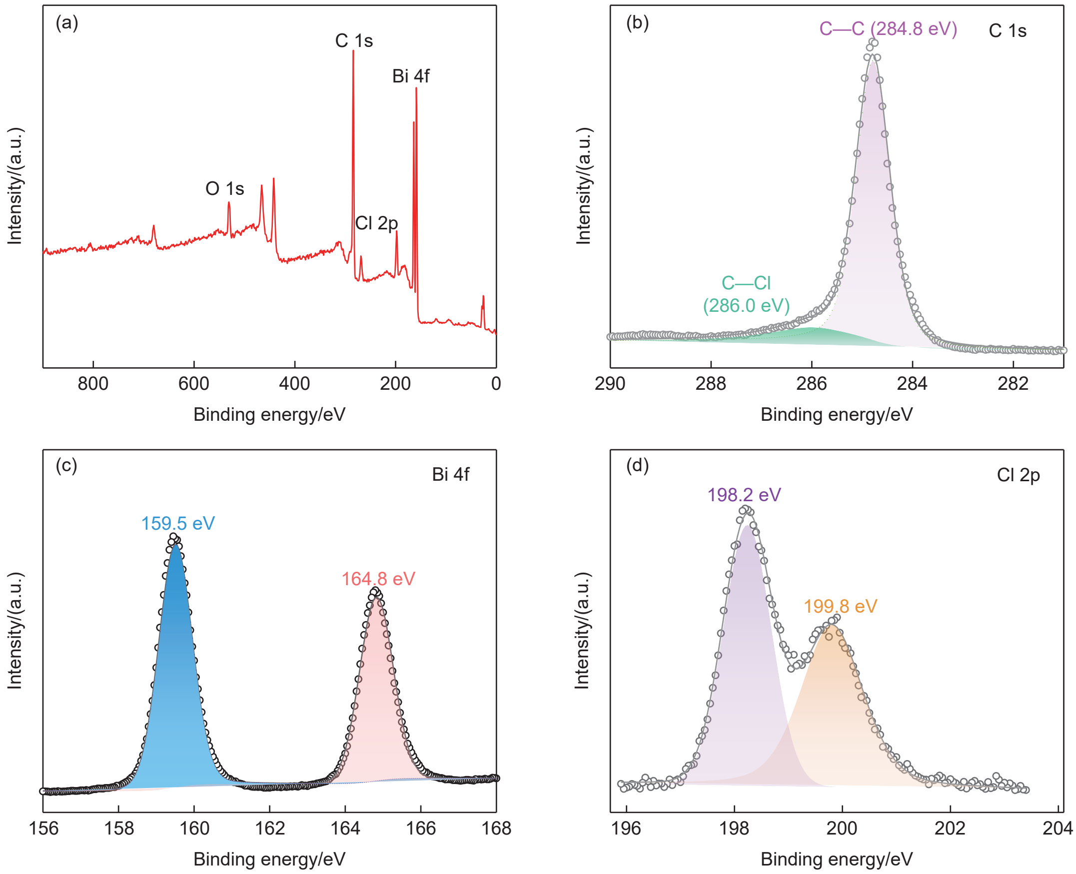

Fig. 3　(a) The full XPS survey spectrum of $BiCl_3$-GICs. High-resolution XPS profiles of (b) C 1s, (c) Bi 4f, and (d) Cl 2p in $BiCl_3$-GICs, respectively

C—Cl bond, respectively[28,30]. In the Bi 4f spectrum (Fig. 3c), the main peaks are located at 159.5 and 164.8 eV, assigned as the Bi $4f_{7/2}$ and Bi $4f_{5/2}$, respectively[31]. The Cl 2p spectrum (Fig. 3d) exhibits 2 apparent peaks at around 198.2 and 199.8 eV, which can be identified as Cl $2p_{3/2}$ and Cl $2p_{1/2}$ signals of Cl^-, indicating that the combination of graphite and chlorine bonds between adjacent graphite layers was well preserved[22].

The morphology of $BiCl_3$-GICs was characterized by the SEM and TEM. The graphite slices is clearly and the lamellar structure is distinctive in the cross section of graphite, where the graphite slices are stacked compactly and neatly (Fig. 4a-b). As expected, the morphology of $BiCl_3$-GICs was similar to that of graphite, indicating that the lamellar structure of graphite remained well preserved (Fig. 4c-d). In addition, there are noticeable lattice stripes with a 1.26 nm spacing that is considerably larger than that of the graphite (0.335 nm) (Fig. 4f), corresponding to the (001) crystal plane of the stage-2 intercalation phase. This is advantageous for lowering the energy barrier of ion diffusion. In addition, the uniform dispersal of C, Cl, and Bi elements can be detected in the element mapping images of $BiCl_3$-GICs sample (Fig. 4g), further certifying the successful insertion of $BiCl_3$ in graphite layers.

The $BiCl_3$ intercalation process was effectively accelerated by employing SO_2Cl_2 as chlorine generator into the reaction system. To verify the universality of this method, the WCl_6-GICs were synthesized by such a SO_2Cl_2-intensified approach. Compared with the *G* peak of graphite, there is a blue shift from 1 580 to 1 611 and 1 623 cm^{-1} for the $MoCl_5$-GICs and WCl_6-GICs, respectively, verifying the successful intercalation of $MoCl_5$ and WCl_6 into graphite layers (Fig. 5a). The sharp peaks at 9.4° and 18.9° for the WCl_6-GICs in the XRD patterns (Fig. 5b) represent the (001) and (002) crystal faces of the stage-1 intercalation phase, respectively. While the sharp peaks at 7.16°, 14.16° and 21.18° for the $MoCl_5$-GICs correspond to the (001), (002) and (003) crystal faces of the stage-2 intercalation phase, respectively. No other discernible diffraction peaks were found, indicating the pure crystal plane of stage-1 intercalation in WCl_6-GICs and the stage-2 intercalation in $MoCl_5$-GICs, which is advantageous to decrease the energy barrier of ion diffusion. The uniform distribution of the C, W and Cl elements in the mapping images of WCl_6-GICs (Fig. 5c) as well as the C, Mo and Cl elements in the mapping images of $MoCl_5$-GICs (Fig. 5d) further certify the successful insertion of WCl_6 and $MoCl_5$ in the graphite layers, respectively. Fig. 5e-f illustrate the cycling performance of the WCl_6-GICs and $MoCl_5$-GICs electrodes, respectively. The WCl_6-GICs exhibit a high specific capacity of 313.34 mAh g^{-1} and an initial coulombic efficiency of 54.8% (Fig. 5e). Following 200 charge/discharge cycles at 1 A g^{-1}, the coulombic efficiency reaches up to 99.0%. The $MoCl_5$-GICs delivers a charge capacity of 379.02 mAh g^{-1} (Fig. 5f). A remarkable capacity of up to 202.83 mAh g^{-1} and a high coulombic efficiency of 99.6% could be observed after 100 cycles, confirming the excellent sodium storing characteristic.

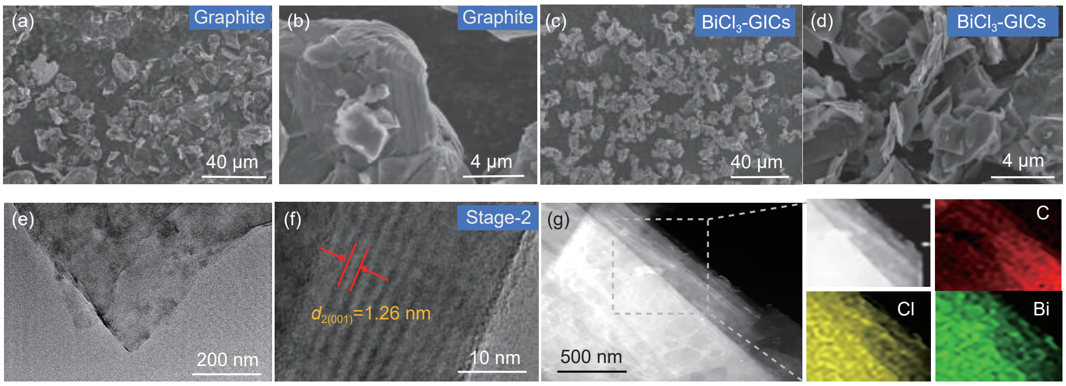

Fig. 4　SEM images of (a-b) graphite and (c-d) $BiCl_3$-GICs. (e-f) TEM images of $BiCl_3$-GICs. (g) The matching mapping images of the elements C, Cl and Bi

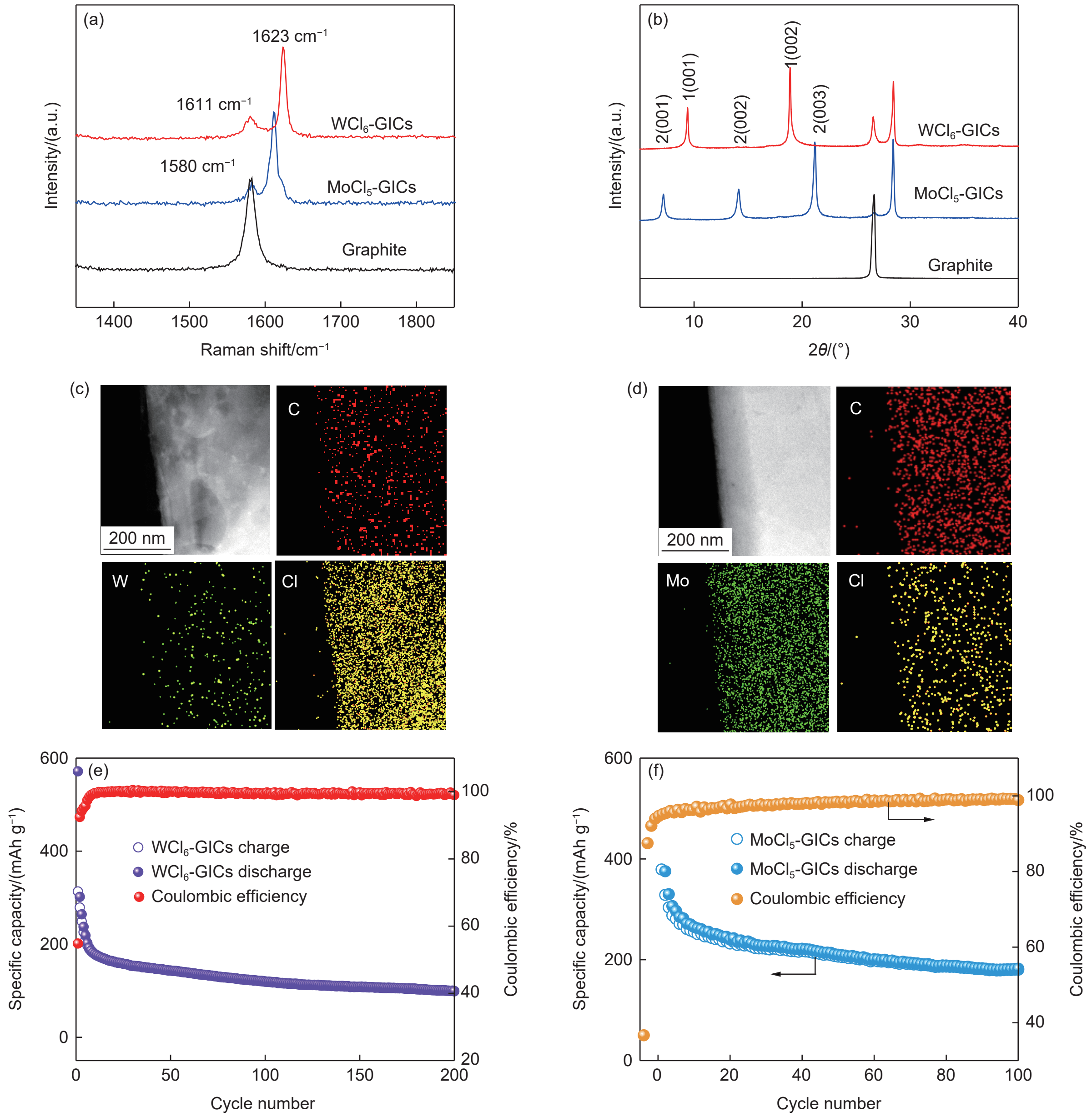

Fig. 5 (a) Raman spectra and (b) XRD patterns of WCl_6-GICs, $MoCl_5$-GICs, and graphite. The elemental mapping images of (c) the C, W and Cl elements in the WCl_6-GICs and (d) the C, Mo and Cl elements in the $MoCl_5$-GICs. Cycling test for (e) WCl_6-GICs and (f) $MoCl_5$-GICs at 1 A g^{-1}

The electrochemical characteristics of the SIB with $BiCl_3$-GICs anode were evaluated by cycling test at 1 A g^{-1}. As shown in Fig. 6a, the SIB delivers a high specific capacity of 247 mAh g^{-1}, much higher than that of graphite (133.6 mAh g^{-1}). This initial 65.3% coulombic efficiency is higher than the value of graphite, which is typically less than 50%[32]. After 100 charge/discharge steps, the Coulombic efficiency is more than 99.5%, implying the fantastic sodium storage property. As shown in Fig. 6b, a pair of redox peaks can be detected in the CV curve of graphite, where the sharp peak at 0.57 V and the broadened peak within the scope of 0.6–0.8 V are assigned to the intercalation/de-intercalation of solvated Na^+ in graphite layers[33], respectively. As for the $BiCl_3$-GICs electrode, the redox peaks can be attributed to the multi-step conversion-alloying reactions among $BiCl_3$ and Na^+[34], leading to capacity much higher than graphite (Fig. 6c). Nevertheless, the peaks corresponding to the intercalation/de-intercalation of Na^+ in graphite layers cannot be detected during the first cycle (Fig. 6d-e), which will be further studied in detail. According to the results of EIS spectra (Fig. 6f), the intrinsic ohmic resistance (R_s) and interfacial charge transfer resist-

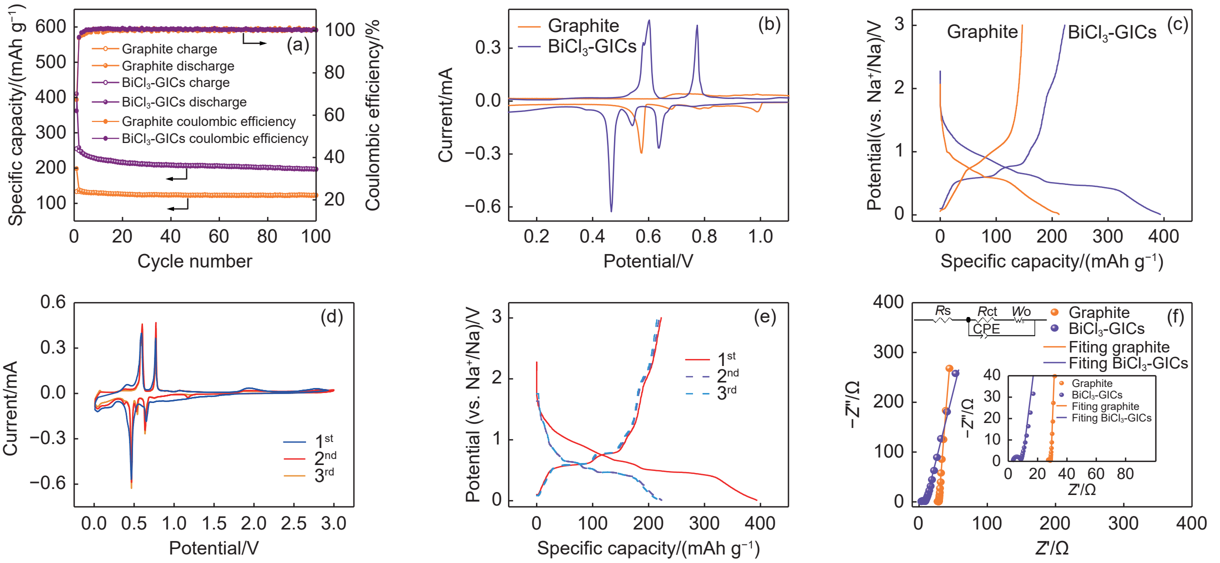

Fig. 6　(a) Cycling performance of BiCl$_3$-GICs and graphite at 1 A g^{-1}. (b) CV curves and (c) GCD curves of graphite and BiCl$_3$-GICs for the first cycle. (d) CV curves and (e) GCD curves of BiCl$_3$-GICs for the first three cycles. (f) EIS curves of BiCl$_3$-GICs and graphite

ance (R_{ct}) of BiCl$_3$-GICs (2.6 Ω for R_s and 5.3 Ω for R_{ct}) are far smaller than that of graphite (20.2 Ω for R_s and 13.4 Ω for R_{ct}), indicating the faster charge transport kinetics of BiCl$_3$-GICs than graphite[35].

Benefiting from the rapid ion transport of BiCl$_3$-GICs, the SIB employing BiCl$_3$-GICs anodes demonstrated a high capacity retention of 80%, *i.e.,* 170 mAh g^{-1} at 5 A g^{-1} compared to 248 mAh g^{-1} at 0.1 A g^{-1} (Fig. 7a-b), which is higher than that of previously reported studies (Fig. 7c)[21,22,34,36]. The excellent rate performance was further explored by the CV tests with different scanning rates (0.1 to 5 mV s^{-1}) (Fig. 7d). In theory, the current (i) of redox peaks and the scanning rates (v) is correlated by following formula[37].

$$i = av^b$$

Here, the reaction kinetic is assessed by the b value. When the value of b gets close to 0.5, the SIB delivers a semi-infinite diffusion behavior, whereas when the value of b approaches 1, the cell exhibits a capacitive behavior. In the CV curves of BiCl$_3$-GICs electrode (Fig. 7d), two anodic and three cathodic peaks are clearly visible. Notably, the amplitude of Peak 2 increased during the cycles, which corresponds to the intercalation of Na$^+$ in graphite layers. In addition, the Peak 3 and Peak 5 are mostly related to the BiCl$_3$ in BiCl$_3$-GICs, where the Peak 5 are the overlapping of reactions in terms of graphite and BiCl$_3$[34]. During the actual charge storage process, the SIB simultaneously shows diffusive and the capacitive behavior. As shown in Fig. 7e-f, the b value of Peak 2 (0.91) indicates the capacitive behavior whereas the b values of Peak 3 and Peak 5 (0.63 and 0.65, respectively) imply the diffusion behavior. The b values of Peak 1 and Peak 4 (0.74 and 0.71, respectively) signify that diffusive and capacitive behavior coexist.

To shed further light on the working principle of BiCl$_3$-GICs anode, in-situ Raman spectroscopy was performed during the first charge/discharge process (Fig. 8). The obvious peaks at 1 612 and 1 582 cm^{-1} were assigned to the stage-2 intercalation phase of BiCl$_3$ and the G peak of the graphite phase, respectively[38]. It was believed that the chlorine atoms occupied the desired sites connected to the graphene lattice when intercalation occurred[39]. During the discharge process, the peak located at 1 612 cm^{-1} shifted to lower wavenumber, suggesting that the ordered structure of BiCl$_3$ in the BiCl$_3$-GICs layer was destroyed as well as the interaction between BiCl$_3$ and graphite was weakened. The BiCl$_3$ underwent a conversion reaction with the Na$^+$ to form Bi and NaCl in the graphite layers between the voltage range from 1.56 to 0.72 V. Subsequently, the G peak of graphite phase shifted from 1 582 to 1 603 cm^{-1} during the progress of discharge, certifying the Na$^+$ doping effect towards graphite layers. Moreover, even though the

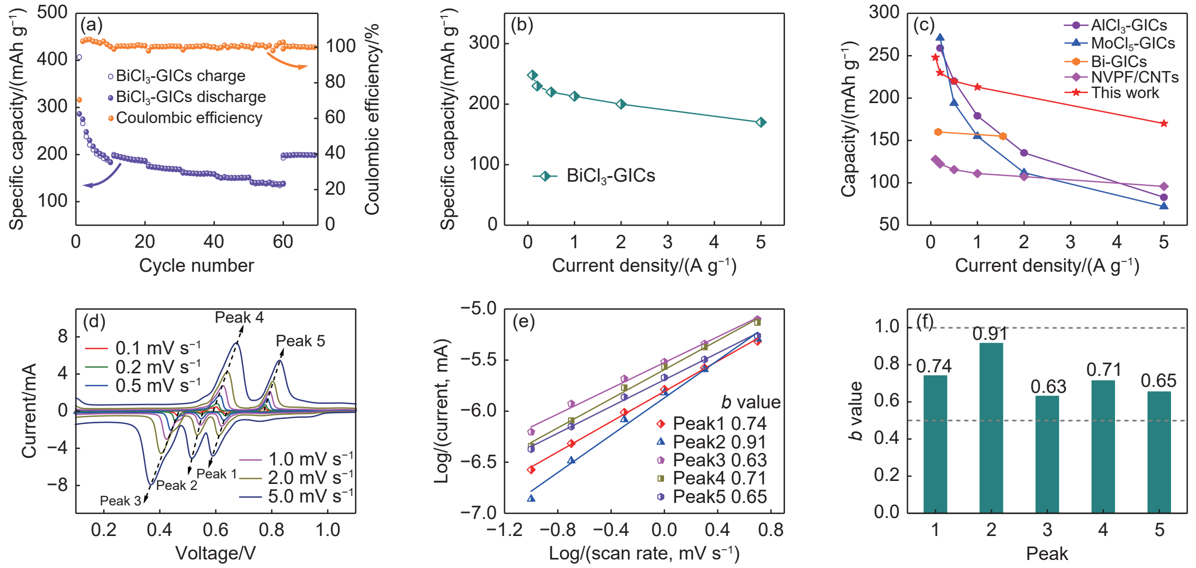

Fig. 7 (a-b) Rate performance of BiCl$_3$-GICs. (c) Comparison of rate performance between this work and the reported SIB anodes. (d) CV curves of BiCl$_3$-GICs at various scan rates. (e) The calculated logarithm connection between scan rate and current based on the CV curves. (f) *b*-values of different redox peaks

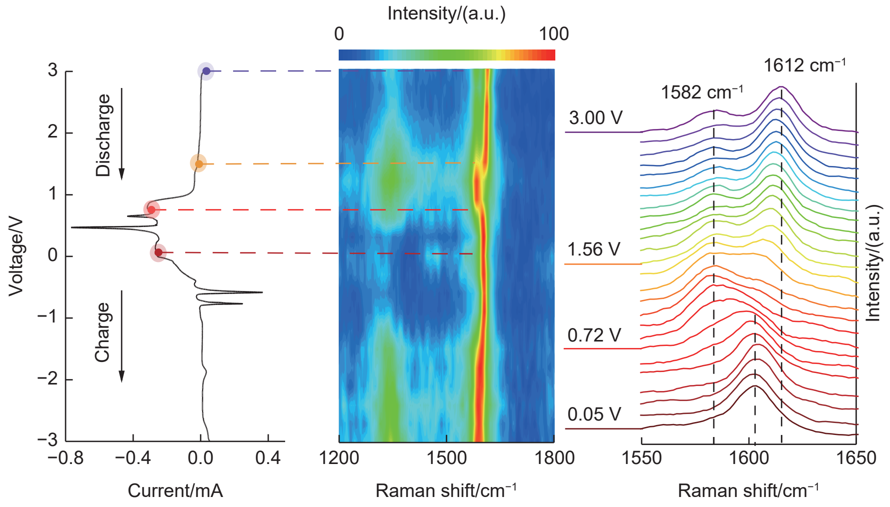

Fig. 8 CV curve for the first charge/discharge process, the *in-situ* Raman mapping and the Raman spectra of BiCl$_3$-GICs electrode

BiCl$_3$ was re-formed after the charging process, the diffraction peak of the BiCl$_3$ stage-2 intercalation phase did not return to the original position, suggesting that the change of BiCl$_3$ was irreversible. To sum up, the disordered transformation of BiCl$_3$ and the weakened electronic interaction between graphite and BiCl$_3$ layer facilitate the exposure of graphite active sites, which endow Na$^+$ intercalation and corresponding peak presence as mentioned above.

4 Conclusions

In summary, an SO$_2$Cl$_2$-intensified intercalation strategy is presented to fabricate the stage-2 phase-dominated BiCl$_3$-GICs with a maximum BiCl$_3$ mass content of 42%. Notably, SO$_2$Cl$_2$ as generator of chlorine molecules could activate BiCl$_3$ molecule and produce reactive intercalated species, thus significantly promoting the intercalation process. As a demonstration, the BiCl$_3$-GICs anodes delivered a higher specific capacity (213 mA h g^{-1}, 1 A g^{-1}) than that of graphite (140 mA h g^{-1}, 1 A g^{-1}) due to the high content of intercalated BiCl$_3$ and enlarged interlayer spacing. Furthermore, the in-situ Raman spectroscopy also shed light on the sodium storage process of BiCl$_3$-GICs electrode. During the initial discharge, the electronic interaction between BiCl$_3$ and graphite was weakened. $BiCl_3$ in the $BiCl_3$-GICs layer underwent disordered change, facilitating the exposure of graphite active sites and the embedding of Na^+ in graphite. As a result, the energy storage capacity and dynamic properties of electrode materials were enhanced. Furthermore, the present strategy is also extended to prepare other metal chloride-intercalated graphite for developing advanced energy storage devices.

Conflicts of interest

The authors declare no conflict of interest.

Acknowledgements

This work was partly supported by the National Key Research and Development Program of China (2022YFB4101600), the Fundamental Research Funds for the Central Universities (DUT22ZD207, DUT22LAB612), and the Shandong Provincial Natural Science Foundation (ZR2023QB095).

References

[1] Li Y, Zhou Q, Weng S, et al. Interfacial engineering to achieve an energy density of over 200 Wh kg^{-1} in sodium batteries[J]. Nature Energy, 2022, 7(6): 511-519.

[2] Tang Z, Zhang R, Wang H, et al. Revealing the closed pore formation of waste wood-derived hard carbon for advanced sodium-ion battery[J]. Nature Communications, 2023, 14(1): 6024.

[3] Yu J, Ren W, Yu C, et al. Enhanced anion-derived inorganic-dominated solid electrolyte interphases for high-rate and stable sodium storage[J]. Energy & Environmental Materials, 2023, 6(4): e12602.

[4] Li S, Qian G, He X, et al. Thermal-healing of lattice defects for high-energy single-crystalline battery cathodes[J]. Nature Communications, 2022, 13(1): 704.

[5] Yang F, Gao H, Chen J, et al. Phosphorus-based materials as the anode for sodium-ion batteries[J]. Small Methods, 2017, 1(11): 1700216.

[6] Fang S, Bresser D, Passerini S. Transition metal oxide anodes for electrochemical energy storage in lithium- and sodium-ion batteries[J]. Advanced Energy Materials, 2020, 10(1): 1902485.

[7] Guo H, Li Y, Wang C, et al. Effect of the air oxidation stabilization of pitch on the microstructure and sodium storage of hard carbons[J]. New Carbon Materials, 2021, 36(6): 1073-1078.

[8] Niu H Z, Wang H H, Sun L Y, et al. N, S co-doped coal-based hard carbon prepared by two-step carbonization and a molten salt template method for sodium storage[J]. New Carbon Materials, 2024, 39(2): 297-307.

[9] Hou Z, Gao Y, Zhang Y, et al. Research progress on freestanding carbon-based anodes for sodium energy storage[J]. New Carbon Materials, 2023, 38(2): 230-243.

[10] Li X, Wang X, Sun J. Recent progress in the carbon-based frameworks for high specific capacity anodes/cathode in lithium/sodium ion batteries[J]. New Carbon Materials, 2021, 36(1): 106-116.

[11] Wang Z, Yu C, Huang H, et al. Carbon-enabled microwave chemistry: from interaction mechanisms to nanomaterial manufacturing[J]. Nano Energy, 2021, 85: 106027.

[12] Wang Z, Yu C, Zhao C, et al. Interface inversion: a promising strategy to configure ultrafine nanoparticles over graphene for fast sodium storage[J]. Small, 2021, 17(1): 2005119.

[13] Xiao J, Han J, Zhang C, et al. Dimensionality, function and performance of carbon materials in energy storage devices[J]. Advanced Energy Materials, 2022, 12(4): 2100775.

[14] Zhao C, Yu C, Qiu B, et al. Ultrahigh rate and long-life sodium-ion batteries enabled by engineered surface and near-surface reactions[J]. Advanced Materials, 2018, 30(7): 1702486.

[15] Zhao C, Yu C, Zhang M, et al. Ultrafine MoO_2-carbon microstructures enable ultralong-life power-type sodium ion storage by enhanced pseudocapacitance[J]. Advanced Energy Materials, 2017, 7(15): 1602880.

[16] Li X, Li J, Ma L, et al. Graphite anode for potassium ion batteries: current status and perspective[J]. Energy & Environmental Materials, 2022, 5(2): 458-469.

[17] Xu Z, Yoon G, Park K, et al. Tailoring sodium intercalation in graphite for high energy and power sodium ion batteries[J]. Nature Communications, 2019, 10(1): 2598.

[18] Huang S, Qiu X, Wang C, et al. Biomass-derived carbon anodes for sodium-ion batteries[J]. New Carbon Materials, 2023, 38(1): 40-66.

[19] Wang Z, Yu C, Huang H, et al. Energy accumulation enabling fast synthesis of intercalated graphite and operando decoupling for lithium storage[J]. Advanced Functional Materials, 2021, 31(15): 2009801.

[20] Wang F, Yi J, Wang Y, et al. Graphite intercalation compounds (GICs): A new type of promising anode material for lithium-ion batteries[J]. Advanced Energy Materials, 2014, 4(2): 1300600.

[21] Li Z, Zhang C, Han F, et al. Towards high-volumetric performance of Na/Li-ion batteries: A better anode material with molybdenum pentachloride-graphite intercalation compounds ($MoCl_5$-GICs)[J]. Journal of Materials Chemistry A, 2020, 8(5): 2430-2438.

[22] Li Z, Tian Z, Zhang C, et al. An $AlCl_3$ coordinating interlayer spacing in microcrystalline graphite facilitates ultra-stable and high-performance sodium storage[J]. Nanoscale, 2021, 13(23): 10468-10477.

[23] Dresselhaus M S, Dresselhaus G. Intercalation compounds of graphite[J]. Advances in physics, 2002, 51(1): 1-186.

[24] Metz W, Shamsrizi M. Investigations of the nucleation process of metal chloride-graphite intercalation compounds[J]. Synthetic Metals, 1989(34): 85-89.

[25] Stumpp E, Niess R. Graphit einlagerungsverbindungen mit thallium(III) chlorid[J]. Carbon, 1978, 16(4): 259-264.

[26] Wang Q, Hui J, Huang Y, et al. The preparation of BiOCl photocatalyst and its performance of photodegradation on dyes[J]. Materials Science in Semiconductor Processing, 2014, 17: 87-93.

[27] Seiler S, Halbig C E, Grote F, et al. Effect of friction on oxidative

graphite intercalation and high-quality graphene formation[J]. Nature Communications, 2018, 9(1): 836.

[28] Xie Z, Zhu Z, Liu Z, et al. Rechargeable hydrogen-chlorine battery operates in a wide temperature range[J]. Journal of the American Chemical Society, 2023, 145(46): 25422-25430.

[29] Cao R, Zhang M, Jiao Y, et al. Co-upcycling of polyvinyl chloride and polyesters[J]. Nature Sustainability, 2023, 6(12): 1685-1692.

[30] Li T, Li M, Li H, et al. High-voltage and long-lasting aqueous chlorine-ion battery by virtue of "water-in-salt" electrolyte[J]. iScience, 2021, 24(1): 101976.

[31] Shi L, Si W, Wang F, et al. Construction of 2D/2D layered g-$C_3N_4/Bi_{12}O_{17}Cl_2$ hybrid material with matched energy band structure and its improved photocatalytic performance[J]. RSC Advances, 2018, 8(43): 24500-24508.

[32] Raccichini R, Varzi A, Wei D, et al. Critical insight into the relentless progression toward graphene and graphene-containing materials for lithium-ion battery anodes[J]. Advanced Materials, 2017, 29(11): 1603421.

[33] Jache B, Adelhelm P. Use of graphite as a highly reversible electrode with superior cycle life for sodium-ion batteries by making use of co-intercalation phenomena[J]. Angewandte Chemie International Edition, 2014, 53(38): 10169-10173.

[34] Chen J, Fan X, Ji X, et al. Intercalation of Bi nanoparticles into graphite results in an ultra-fast and ultra-stable anode material for sodium-ion batteries[J]. Energy & Environmental Science, 2018, 11(5): 1218-1225.

[35] Wang C, Wang L, Li F, et al. Bulk bismuth as a high-capacity and ultralong cycle-life anode for sodium-ion batteries by coupling with glyme-based electrolytes[J]. Advanced Materials, 2017, 29(35): 1702212.

[36] Lei L, Sun K, Hongwei Z, et al. Large scale preparation of $Na_3V_2(PO_4)_2F_3$ with cross-linked double carbon network for high energy density sodium ion batteries at −20 °C[J]. Journal of Energy Storage, 2024, 78: 109923.

[37] Dong X, Chen L, Liu J, et al. Environmentally-friendly aqueous Li (or Na)-ion battery with fast electrode kinetics and super-long life[J]. Science Advances, 2016, 2(1): e1501038.

[38] Wang J, Song X, Yu C, et al. A ferricyanide anion-philic interface induced by boron species within carbon framework for efficient charge storage in supercapacitors[J]. ACS Applied Materials & Interfaces, 2024, 16(10): 12916-12923.

[39] Zhao W, Tan P H, Liu J, et al. Intercalation of few-layer graphite flakes with $FeCl_3$: Raman determination of fermi level, layer by layer decoupling, and stability[J]. Journal of the American Chemical Society, 2011, 133(15): 5941-5946.